LANGMUIR

Article

pubs.acs.org/Langmuir

Pore Size Effect on Methane Adsorption in Mesoporous Silica Materials Studied by Small-Angle Neutron Scattering

Wei-Shan Chiang,[†,‡] Emiliano Fratini,[§] Piero Baglioni,[§] Jin-Hong Chen,*[,∥] and Yun Liu*[,†,‡]

[†]Center for Neutron Research, National Institute of Standards and Technology, Gaithersburg, Maryland 20899, United States

[‡]Department of Chemical and Biomolecular Engineering, University of Delaware, Newark, Delaware 19716, United States

[§]Department of Chemistry "Ugo Schiff" and CSGI, University of Florence, via della Lastruccia 3-13-Sesto Fiorentino, I-50019 Florence, Italy

[∥]Aramco Services Company, Aramco Research Center-Houston, Texas 77096, United States

Supporting Information

ABSTRACT: Methane adsorption in model mesoporous silica materials with the size range characteristic of shale is studied by small-angle neutron scattering (SANS). Size effect on the temperature-dependent gas adsorption at methane pressure about 100 kPa is investigated by SANS using MCM-41 and SBA-15 as adsorbents. Above the gas−liquid condensation temperature, the thickness of the adsorption layer is found to be roughly constant as a function of the temperature. Moreover, the gas adsorption properties, such as the adsorbed layer thickness and the specific amount of adsorbed gas, have little dependence on the pore size being studied, i.e., pore radius of 16.5 and 34.1 Å, but are mainly affected by the roughness of the pore surfaces. Hence, the surface properties of the pore wall are more dominant than the pore size in determining the methane gas adsorption of pores at the nanometer size range. Not surprisingly, the gas−liquid condensation temperature is observed to be sensitive to pore size and shifts to higher temperature when the pore size is smaller. Below the gas−liquid condensation temperature, even though the majority of gas adsorption experiments/simulations have assumed the density of confined liquid to be the same as the bulk density, the measured methane mass density in our samples is found to be appreciably smaller than the bulk methane density regardless of the pore sizes studied here. The mass density of liquid/solid methane in pores with different sizes shows different temperature dependence below the condensation temperature. With decreasing temperature, the methane density in larger pores (SBA-15) abruptly increases at approximately 65 K and then plateaus. In contrast, the density in smaller pores (MCM-41) monotonically increases with decreasing temperature before reaching a plateau at approximately 30 K.

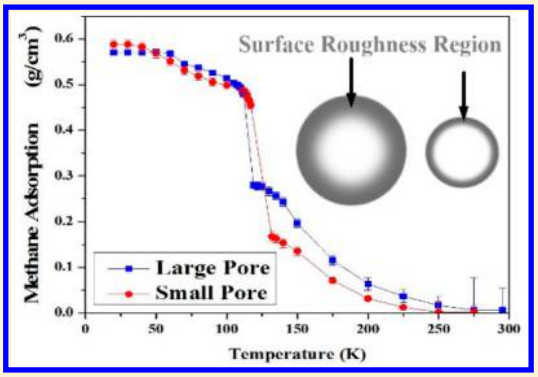

INTRODUCTION

There has been increasing research on the pore morphology of shale rocks due to the success in extracting hydrocarbons from shale reservoirs.[1−3] Shale gas production has increased from 9.6 billion cubic meter (bcm) in 2001 to 282 bcm in 2015 in the U.S.[4] and became the largest share of U.S. natural gas production in 2013.[5] Nevertheless, many fundamental problems related to the storage and transportation of gas in shales are still lacking in understanding. Kerogen is the organic component in the shales that does not dissolve in any solvent, and it imbeds within the inorganic matrix in the rocks. The predominant hydrocarbons in the shale rocks have been found to be stored within the kerogen which has pores with the characteristic length scale between 1 and 100 nm.[6,7] To better estimate the total gas in place (GIP) and the gas transportation properties in the shale rocks, it is necessary to understand the adsorption properties of natural gas, especially methane, in nanopores of different pore sizes and surface properties. For nanometer-sized pores, the pore surface properties can play essential roles of gas adsorption and flow modulator. The total hydrocarbon reserve is the summation of hydrocarbon adsorbed on the pore surface and the free gas in the pore.[6]

Ordered mesoporous silicas have drawn much attention since their discovery in the early 1990s. They have been demonstrated to have outstanding applications in gas storage, separation processes, and heterogeneous catalysis.[8−12] These materials have relatively large surface area and uniform pore size. Moreover, the ability to tailor their pore size in a wide range from about 2 nm up to 30 nm,[13] which covers the characteristic pore size in kerogen and shale rocks, makes them suitable model adsorbents to study shale gas adsorption. Adsorption isotherm measurements for gases such as N_2 and Ar have been widely used to study the mesoporous silica materials such as MCM-41 and SBA-15.[14,15] As a complementary

Received: June 20, 2016
Revised: August 9, 2016
Published: August 11, 2016

DOI: 10.1021/acs.langmuir.6b02291
Langmuir 2016, 32, 8849−8857

technique, X-ray diffraction has been applied to investigate the structure change during gas adsorption for Ar,[16,17] Kr,[18] and C_5F_{12}[19] on MCM-41 and SBA-15. However, there are few studies on the adsorption mechanism of the most common component in natural gas, methane, on these mesoporous silicas. Methane adsorption behaviors on these model materials with well-controlled pore size and surface chemistry can provide essential information for the petroleum industry with interest in producing natural gas from shales to understand the transportation and storage of methane gas within the nanopores characteristic of the real rocks.

Gas adsorption on mesopores begins with the adsorption of gas molecules on the surface before the capillary condensation pressure or temperature.[20,21] This vapor−liquid condensation is a first-order phase transition. When it takes place, the pores are fully filled with confined fluid. Many studies have shown that the fluid under confinement of nanometer size scale has thermodynamic properties different from the properties of bulk fluids.[22−25] In particularly, Jiang et al.[23] studied the phase transition of *n*-alkanes from methane to *n*-butane in carbon nanotubes using gauge-cell Monte Carlo method and found that the critical temperature is decreased, the critical density is increased, and the binodal curve is narrowed. Tan and Piri[24] used perturbed-chain statistical associating fluid theory (PC-SAFT) coupled with the Young−Laplace equation to calculate the confined fluid phase behavior in nanopores and reported that at critical temperature, surface tension and saturated density of confined phases are shifted from those of bulk phases. Gor et al.[22] carried out two different simulation methods and showed that compressibility of confined fluid changes linearly with pore size. So far most of the structural investigations on natural gas adsorbed in confined state were based on theory and simulation.[23,24,26−28] There is an urgent need for experimental verification of the hydrocarbon properties confined in the nanopores under the influences of pore size, surface chemistry, pore structure, etc., so that the understanding of natural gas behaviors in the shale rocks or other porous materials can be advanced.

In this study, two mesoporous silicas, MCM-41 and SBA-15, are chosen in order to study the pore size effect on the gas adsorption process of methane. MCM-41 and SBA-15 have cylindrical mesopores with narrow pore size distributions packed into two-dimensional *p6mm* hexagonal space group. It is known that increasing the pore size increases the capillary condensation pressure at a given temperature.[29−31] For the same porous material, increasing the isotherm temperature increases the capillary condensation pressure.[32,33] Kruk and Jaroniec[30] studied argon adsorption isotherms at 77 K on MCM-41 and SBA-15 with various pore sizes and claimed that below the capillary condensation pressure, the adsorbed film thickness increases with decreasing pore size. But when the pore size is above 4 nm, the film thickness shows little correlation with the pore size. The increase in adsorbed layer thickness with decrease in pore size is also found in N_2 adsorption isotherms for MCM-41 with pore diameter from 24.0 to 49.2 Å.[29,31] Qiao et al.[32] carried on hexane adsorption isotherms on MCM-41 with different size, and they found an almost constant thickness of adsorbed hexane layer before capillary condensation when pore diameter is larger than 24.0 Å. However, these studies relied on the volumetric measurement methods and assumed that the pores have smooth surfaces. The structural information is inferred based on the used models.

It has been shown that the surface of the pores cannot be assumed to be smooth. The change of the surface properties can significantly influence the gas adsorption. Previous studies on MCM-41 and SBA-15 by X-ray diffraction and neutron scattering indicated that their pore walls are diffusive rough interfaces rather than smooth and sharp interfaces.[16,18,19,34] Our previous study[34] showed that due to the rough pore surface of SBA-15, the amount of methane adsorption on the pore surface is more than half of the amount of all liquid methane fully filling the pore volume at the gas−liquid condensation temperature. The surface roughness comes from the morphological defects such as corrugated pore wall and microporosity.[35,36] Density functional theory (DFT)[16] and grand canonical Monte Carlo (GCMC) simulation[36] were also applied to investigate the surface roughness of MCM-41, and by taking into account the pore wall roughness of MCM-41, the simulated gas adsorption curves have reproduced the experimental Ar adsorption curves. Therefore, it is important to elucidate the pore size effect by taking into consideration the surface roughness of the pore wall to obtain the detailed structure change upon gas adsorption process and separate the pore size and surface roughness impacts in order to elucidate the key factors that determine the total hydrocarbon reserve.

In this study, we investigate the methane gas adsorption in mesporous silica materials with two different pore sizes as a function of the temperature by using small-angle neutron scattering (SANS). Surface roughness is also taken into account to assess its effect on the gas adsorption. The adsorption of deuterated methane is carried out at pressure ≈100 kPa (close to isobar condition) on MCM-41 and SBA-15. The previously developed scattering models and methods[34] are used to extract the essential adsorption properties such as the thickness of the adsorption layer, the mass density of CD_4 under confinement, and the total gas storage within the pores. It is worth noting that there are only very few isobar[34,37−39] gas adsorption studies compared with isotherm adsorption investigations. Especially, most of isobar studies focus on chemisorption[38,39] rather than physisorption as in the case of methane adsorption in silica materials. To the best of our knowledge, this is the first SANS study of pore size effect on temperature-dependent gas adsorption.

MATERIALS AND METHODS

Materials. *Synthesis of MCM-41.* Mesoporous silica MCM-41 was synthesized following the methodology reported by Ritter et al.[40] The structure-directing agent used was hexadecyltrimetilammonium bromide (CTAB, Sigma[41]). CTAB (8.8 g) was dissolved in a mixture of 208 mL of distilled water and 96 mL of aqueous NH_3 (Sigma-Aldrich[41]) at 35 °C. Then 40 mL of tetraethyl orthosilicate (TEOS, Sigma[41]) was slowly added to this clear solution under stirring, and the solution was kept at these conditions for 3 h. Then the gel was aged at room temperature for 24 h in a Teflon bottle. The product was separated by centrifugation, washed with deionized water until the pH value of the washing solution was neutral, and dried in air at room temperature. In order to remove the surfactant occluded in the mesopores, the synthesized material was calcined in static air at 550 °C for 4 h.

Synthesis of SBA-15. Mesoporous silica SBA-15 was synthesized following the approach reported by Zhao et al.[42] The structure-directing agent and the silicon source used are the commercial triblock copolymer (Pluronic P123, Sigma[41]) and TEOS, respectively. P123 (6 g) was dissolved in 45 mL of

DOI: 10.1021/acs.langmuir.6b02291
Langmuir 2016, 32, 8849−8857

deionized water and 150 mL of 2 M hydrochloric acid at 35 °C, where M represents mol/L, and the solution was stirred vigorously. TEOS (13.8 mL) was then added dropwise to the solution. The synthesis gel was aged for 24 h. The gel was then hydrothermally treated at 80 °C for another 24 h in a Teflon bottle. The precipitated product was centrifuged, washed with deionized water until the pH value of the washing solution became neutral, and dried overnight at 80 °C. The surfactant molecules were removed by annealing the white powder at 550 °C for 4 h.

The final MCM-41 and SBA-15 powder were tested by N_2 adsorption isotherm measurement, and the textural properties are summarized in Table 1. The adsorption isotherm for N_2 on both samples can be found in Figure S4 of the Supporting Information. It is known that the pore size estimated using N_2 isotherm by the BJH method may not be accurate.[43] The pore size and its surface structure of our samples are determined by neutron scattering methods, which are discussed later in this paper.

Table 1. Properties of MCM-41 and SBA-15 Obtained from N_2 Isotherm Measurement

material	BET surface area (m^2/g)	pore size[a] (Å)	pore volume (mL/g)
MCM-41	956.76	39.0	0.8557
SBA-15	781.15	60.6	0.8198

[a]Estimated with the adsorption branch of the isotherm, using the BJH method.

Small-Angle Neutron Scattering (SANS). Small-angle neutron scattering (SANS) measurements were conducted at *n*Soft-10m SANS and NGB-30m SANS at the National Institute of Standards and Technology (NIST) Center of Neutron Research (NCNR). The incident neutron wavelength, λ, was chosen to be 5 or 6 Å, and the sample-to-detector distances, SSDs, were selected to cover a scattering vector (q) range from 0.004 to 0.596 $Å^{-1}$. All SANS data were corrected for the sample transmission, the background scattering, and the detector sensitivity to obtain the absolute intensity based on a standard procedure described elsewhere.[44]

MCM-41 and SBA-15 samples were degassed at 120 °C for 1.5 h before the SANS experiment. The degassed samples were loaded in aluminum sample cells with 1 mm path length. The temperature of the samples was controlled by a closed cycle refrigerator (CCR). Deuterated methane (CD_4, Cambridge Isotope Laboratories, Inc.[41]) was loaded by a gas loading line linked between the sample cell and a CD_4 gas cart mounted with a pressure sensor. SANS measurement was first conducted on MCM-41 and SBA-15 under vacuum. CD_4 gas was then loaded in situ to the sample cell. SANS measurements were performed at temperatures ranging from 20 to 295 K. The amount of the sample in each cell was maintained the same during the experiments. The CD_4 pressure was monitored and maintained at about 100 kPa by the CD_4 gas cart at temperature above the lowest temperature of capillary condensation temperature range ($T_{c,L}$). The slight change of CD_4 pressure at $T > T_{c,L}$ can be found in Figure S3 in the Supporting Information. At $T < T_{c,L}$, the valve connecting the CD_4 gas cart and the sample cell was closed to prevent further condensation of gas in the bulk phase.

SANS DATA ANALYSIS

In previous work,[34] we have developed a theoretical model to understand the scattering intensity for the hexagonally packed cylindrical mesopores without or with gas loaded inside. The small-angle scattering intensity $I(q)$ of powder MCM-41 or SBA-15 with CD_4 loaded (we refer it as CD_4/MCM-41 or CD_4/SBA-15 in the remainder of the paper) can be expressed as

$$\lim_{q_{h,k}L\to\infty} I(q_{h,k}) = C\sum_{h,k}\left\{\frac{1}{q_{h,k}}m_{h,k}\times\left[\rho_{ads}R_m^2\frac{2J_1(q_{h,k}R_m)}{q_{h,k}R_m}\exp\left[-\frac{(\sigma q_{h,k})^2}{2}\right] - \rho_{ads}2\pi^2R_v^2R_m^2\times\int_0^{2\pi}d\delta'\int_0^{\infty}dq_r'q_r'\frac{2J_1(q_r'R_m)}{q_r'R_m}\exp\left[-\frac{(\sigma q_r')^2}{2}\right]\frac{2J_1\left(\sqrt{q_{h,k}^2+q_r'^2-2q_{h,k}q_r'\cos(\delta')}\,R_v\right)}{\sqrt{q_{h,k}^2+q_r'^2-2q_{h,k}q_r'\cos(\delta')}\,R_v} - \rho_mR_m^2\frac{2J_1(q_{h,k}R_m)}{q_{h,k}R_m}\exp\left[-\frac{(\sigma q_{h,k})^2}{2}\right]\right]^2\right\} \quad (1)$$

J_1 is the first-order Bessel function. R_m is the nominal radius of matrix pore and R_v is the radius of CD_4 vapor core. ρ_v, ρ_{ads}, and ρ_m are neutron scattering length densities (SLDs) of the CD_4 vapor core, adsorbed CD_4, and SiO_2 matrix, respectively (see Figure 1 in ref 34). In the temperature and pressure ranges being studied, ρ_v is small compared with ρ_{ads}, and therefore ρ_v is set to be zero. σ is the diffusive parameter characterizing the surface roughness of the mesopore wall. $m_{h,k}$ is the multiplicity, and C is a constant prefactor related to the length L and number density of the cylindrical mesopores. If the amount of sample inside the neutron beam is the same during scattering measurements, C is independent of the temperature. Equation 1 is derived under the assumption that the interface between the silica matrix and the adsorbed layer is diffusive interface while the interface between the adsorbed layer and vapor core is sharp interface.[34]

For empty matrix, there is no adsorbed layer and the mesopores are under vacuum and therefore R_v and ρ_{ads} are zero. When mesopores are fully filled with methane liquid or solid, R_v is zero and ρ_{ads} becomes the SLD of confined liquid or solid methane. In both cases, eq 1 reduces to

$$\lim_{q_{h,k}L\to\infty} I(q_{h,k}) = C\sum_{h,k}\left\{\frac{1}{q_{h,k}}m_{h,k}\left[\rho R_m^2\frac{2J_1(q_{h,k}R_m)}{q_{h,k}R_m}\exp\left[-\frac{(\sigma q_{h,k})^2}{2}\right]\right]^2\right\} \quad (2)$$

DOI: 10.1021/acs.langmuir.6b02291
Langmuir 2016, 32, 8849−8857

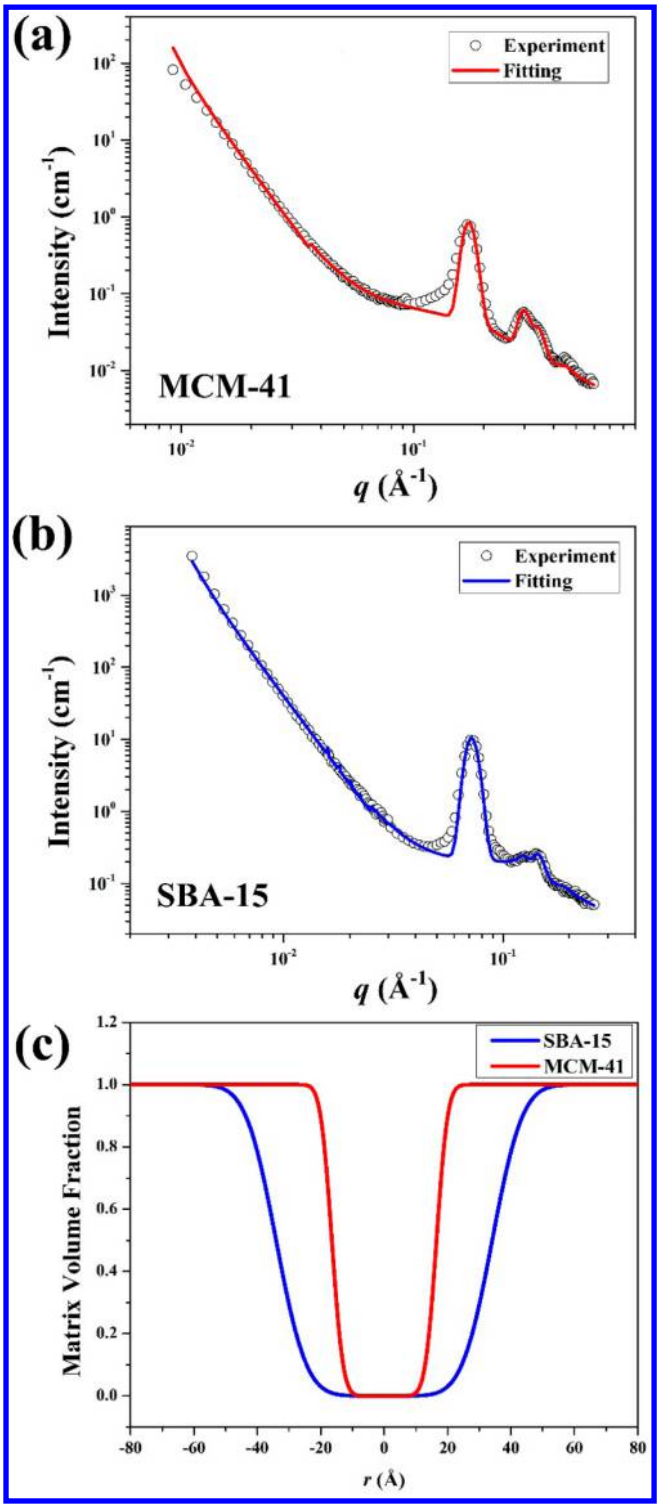

Figure 1. SANS data (open circle) and the corresponding fitting curve (solid line) for (a) MCM-41 and (b) SBA-15. (c) Radial distribution of the volume fraction of the SBA-15 (blue line) and MCM-41 (red line) matrices. Error bars in (a) and (b) represent one standard deviation and are smaller than the symbols.

$\rho = \rho_m$ and $\rho = (\rho_{CD_4} - \rho_m)$ for empty mesopore and fully filled mesopores, respectively. ρ_{CD_4} is the SLD of liquid or solid CD_4 that fills the entire mesopores.

The measured SANS intensity $I_M(q)$ can be calculated after considering the instrument resolution function

$$I_M(q) = \int \frac{I(q')}{\sqrt{2\pi\delta(q)^2}} \exp\left[-\frac{(q - q_m)^2}{2\delta(q)^2}\right] dq'$$

where $I(q')$ is the theoretical intensity calculated through eq 1 with q' as a dummy variable. The SANS instrument resolution is approximated as a Gaussian function with the standard deviation $\delta(q)$ and q dependent parameter q_m.

The structural information on empty MCM-41 and SBA-15 without loading any gas is first obtained by fitting the SANS data using eq 2. ρ_m (SLD of silica matrix) is a known parameter determined by separate contrast variation SANS measurements, and the details are described in the Supporting Information. ρ_m is $(3.66 \pm 0.009) \times 10^{10}$ cm^{-2} for MCM-41 and $(3.51 \pm 0.008) \times 10^{10}$ cm^{-2} for SBA-15, where the confidence intervals for uncertainties represent one standard deviation. The fitting parameters in eq 2 are prefactor C, nominal pore radius R_m, and diffusive parameter σ. Once the parameters of the solid matrix C, R_m, and σ are determined, they are fixed as known parameters for gas loading cases. The only fitting parameters in eq 1 for CD_4/MCM-41 and CD_4/SBA-15 are ρ_{ads}, R_v, and the background. The details of fitting procedure can be found in the previous work.[34]

RESULTS AND DISCUSSION

Properties of Empty MCM-41 and SBA-15. Figure 1a and 1b show the SANS experimental data and the best fits using eq 2 for empty MCM-41 and SBA-15, respectively. The scattering patterns for both cases show clearly the first-order diffraction peak and overlapped second- and third-order peaks. For MCM-41, even the fourth peak can be seen. The peak positions indicate both MCM-41 and SBA-15 have the *p6mm* hexagonal symmetry of the mesopores. The structural fitting parameters for the silica matrices from SANS fitting are listed in Table 2. The nominal pore radius R_m of SBA-15 is about twice that of R_m of MCM-41. The normalized surface roughness parameter σ/R_m is larger for SBA-15 likely due to the large microporosity of its pore wall which has been documented in the literature.[35,45] Figure 1c shows the volume fraction distribution, $\varphi_m(r)$, for the empty silica matrix of MCM-41 and SBA-15 calculated by the extracted fitting parameters listed in Table 2. In the center the mesopores are under vacuum, and $\varphi_m(r)$ is zero. The pore wall is not a sharp interface but a smooth diffuse interface characterized by the diffuse parameter σ.

Temperature-Dependent Gas Adsorption. Figure 2 shows the SANS data for gas loading matrices for (a) CD_4/MCM-41 and (b) CD_4/SBA-15[34] at different temperatures. The relative intensity of the peaks changes significantly with temperature. Separate measurements for empty silica matrices without loading gas at the same temperature range have been conducted, and they confirm that the structures of the matrices are stable and do not change within the temperature range being studied (see Figure S2 in the Supporting Information). Therefore, the intensity changes shown in Figure 2 are solely due to the CD_4 gas loaded inside the matrices.

Figure 3a indicates the first-order peak intensity as a function of temperature for both CD_4/MCM-41 and CD_4/SBA-15. The intensity is normalized to the first-order peak intensity at 295 K for each case and has similar trend for both cases. At high temperature, the first peak intensity increases with decreasing temperature because CD_4 molecules are gradually adsorbed into the surface of the pores and form a dense region on the

DOI: 10.1021/acs.langmuir.6b02291
Langmuir 2016, 32, 8849−8857

Table 2. Textural Properties of MCM-41 and SBA-15 Obtained from SANS Data Analysis

material	$a^{a,b}$ (Å)	$\rho_m{}^{a,c}$ (10^{10} cm^{-2})	$R_m{}^{a}$ (Å)	σ^{a} (Å)	σ/R_m
MCM-41	42.1	3.66 ± 0.009	16.5 ± 0.1	2.8 ± 0.2	0.17
SBA-15	100.4	3.51 ± 0.008	34.08 ± 0.05	7.51 ± 0.09	0.22

[a]The confidence intervals for uncertainties of the fitting parameters represent one standard deviation. [b]Calculated by $\frac{4\pi}{\sqrt{3}q_{max}}$, where q_{max} is the first-order peak position and fixed as a known parameter during the fitting procedure. [c]Determined by separate contrast variation SANS measurements described in the Supporting Information.

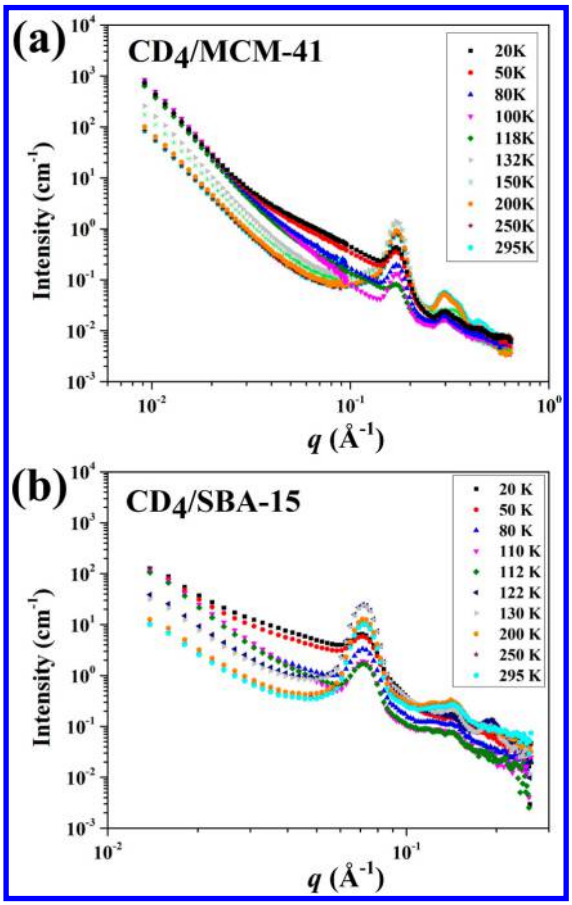

Figure 2. Temperature-dependent SANS data at pressure ≈100 kPa for (a) CD_4/MCM-41 and (b) CD_4/SBA-15. Error bars represent one standard deviation and are smaller than the symbols.

pore surface. The intensity drops dramatically for both cases when the gas–liquid condensation happens and CD_4 vapor condenses into liquid and fills the entire mesopores. Our results clearly indicate that the condensation temperature (T_c) is higher for MCM-41 which has smaller pores than SBA-15. Below T_c, the intensity increases again if further decreasing the temperature because the density of liquid CD_4 confined in the pores increases and eventually CD_4 becomes solid.

The structural parameters of CD_4/MCM-41 and CD_4/SBA-15 are extracted by fitting the SANS data in Figure 2 using eq 1. The first peak intensity calculated from the extracted parameters giving the best fits is plotted together with the experimental peak intensity in Figure 3a. Figure 3a indicates that our model can reproduce the change of SANS data with the temperature very well. Figure 3b shows the vapor core radius R_v as a function of temperature. R_v decreases slightly with decreasing temperature when $T > T_c$ but roughly maintains as a constant value for both CD_4/MCM-41 and CD_4/SBA-15. The relative constant value of R_v above T_c for both cases indicates the region of the surface adsorption is not changed too much with the decreasing temperature even though the amount of gas adsorbed inside this region keeps increasing. If the matrix boundary is set to be $R_m + 2\sigma$, the average adsorbed layer thickness is estimated to be 7 and 9 Å for CD_4/MCM-41 and CD_4/SBA-15, respectively. The similar layer thickness despite the large difference in the pore size between MCM-41 and SBA-15 indicates that the layer thickness is dominated by the surface properties such as surface roughness and surface chemistry. Since both MCM-41 and SBA-15 matrices are composed of SiO_2, the interaction between the pore wall and the CD_4 molecules should be similar for both cases. The increase in layer thickness with the decrease of pore size discussed in some literature[29−31] is not clearly observed in our study.

The existence of the rough surface regions in the studied mesoporous materials changes the gas adsorption properties compared to materials with only smooth pore surfaces. Thus, this brings a challenge when studying the pore size effect on gas adsorption using the volumetric isotherm adsorption in model porous materials where the surfaces were usually assumed to be smooth without any roughness.[29,30,32] For example, for N_2 adsorption on MCM-41, Qiao et al.[29] reported that the layer thickness at the relative pressure of 0.2 increases from ≈5 Å to ≈6 Å if mesopore diameter decreases from 49.2 to 30.4 Å by assuming a smooth surface in the materials. This layer thickness difference is much smaller than the thickness of the surface regions in both cases studied here. If considering the pore outer boundary as $r = R_m + 2\sigma$ and the thickness of pore wall roughness region as 2σ, the thickness of the rough surfaces for MCM-41 and SBA-15 is 5.6 and 15.0 Å, respectively, in our samples. According to our analysis, for SBA-15 (nominal diameter D_m = 68 Å) and MCM-41 (D_m = 32 Å), the thickness detected in previous study is actually within the surface roughness region. Therefore, even if there is some difference of adsorption layer thickness due to the pore size variation, it is a secondary effect because of the existence of the roughness region of the pore wall. The region of the rough surface extends from $R_m - 2\sigma$ to $R_m + 2\sigma$ (Figure 1c). The total roughness region is at 11 Å < r < 22 Å and at 19 Å < r < 49 Å in the mesopores of MCM-41 and SBA-15, respectively. This is actually quite wide. If the pore outer boundary is at $R_m + 2\sigma$, the adsorbed methane layer with thickness ≈7 Å covers 15 Å < r < 22 Å in the mesopores of MCM-41, and that with thickness ≈9 Å covers 40 Å < r < 49 Å in the mesopores of SBA-15 (Figure 3b). Therefore, for both MCM-41 and SBA-15, the adsorbed layer of methane does not fully cover the surface roughness region before the capillary condensation happens.

When $T < T_c$, we can determine the average density of liquid and solid CD_4 confined in the mesopores. Since liquid or solid fills the entire pores, we fix R_v to be zero during the fitting process when $T < T_c$. It should be noticed that in these fittings, there is only one fitting parameter, that is, the scattering length

DOI: 10.1021/acs.langmuir.6b02291
Langmuir 2016, 32, 8849−8857

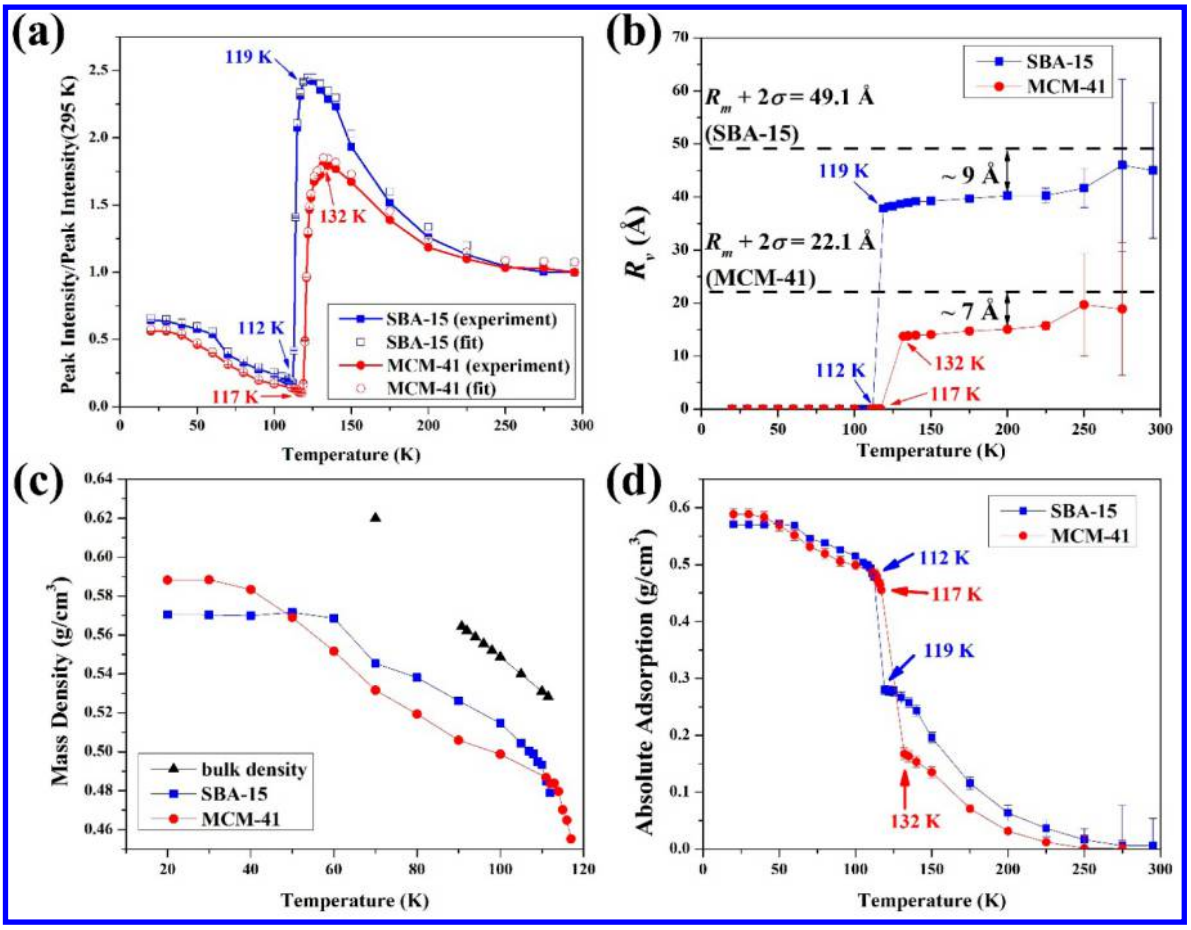

Figure 3. (a) First-order peak intensity of experimental (solid) and fitting (open) data, (b) vapor core radius (R_v), (c) CD_4 mass density, and (d) absolute adsorption per volume for SBA-15 (blue square) and MCM-41 (red circle) as a function of temperature. The lines are only guides to the eye, and error bars represent one standard deviation. CD_4 pressure is maintained ≈100 kPa.

density of the liquid/solid methane, ρ_{CD_4}, in the mesopores (see eq 2). The mass density of confined CD_4 can be calculated from the extracted ρ_{CD_4} through the following equation: $\rho_{CD_4} = \frac{\rho_{CD_4,mass}}{M_w} N_A b$. $\rho_{CD_4,mass}$ is the mass density of CD_4, M_w is the molecular weight of CD_4 (= 20 g/mol), b is the total bound coherent scattering length of one CD_4 molecule (= 3.33×10^{-4} Å), and N_A is Avogadro's constant. The mass density of CD_4 under confinement of both MCM-41 and SBA-15 extracted from SANS results together with bulk CD_4 density at the corresponding temperature at 100 kPa are plotted in Figure 3c. Bulk density of deuterated methane is simply obtained from $\rho_{CD_4,mass} = \rho_{CH_4,mass} \times \frac{M_{w,CD_4}}{M_{w,CH_4}}$, where $\rho_{CD_4,mass}$ and $\rho_{CH_4,mass}$ are the mass density of CD_4 and CH_4, and M_{w,CD_4} = 20 g/mol and M_{w,CH_4} = 16 g/mol are molecular weight of CD_4 and CH_4, respectively. The bulk density of CD_4 using the literature results of CH_4[46] is appreciably higher than the density of the CD_4 confined in the nanometer-sized pores studied here. If we assume the bulk density as the confined methane density, the calculated scattering intensity is much higher than the measured intensity which can definitely be distinguished by the instrument. Notice that the accuracy of the obtained methane density in MCM-41 and SAB-15 critically depends on the accuracy of the SLD of the matrix. In the Supporting Information, we show that the matrix SLD can be accurately determined by the contrast variation experiments. Therefore, we ensure that the confined methane density in the nanopores in the temperature and pressure conditions studied here is lower than the bulk density even though the difference is not large. Our results are consistent with the calculation from perturbed-chain statistical associating fluid theory (PC-SAFT) coupled with Young−Laplace equation done by Tan and Piri.[24] They showed that CO_2 and *n*-pentane densities in confined MCM-41 with radius of 22.0 and 22.9 Å, respectively, are smaller than the corresponding bulk density. It is an interesting finding that density of confined liquid is slightly smaller than density of bulk liquid. For the commonly used volumetric (Sieverts' method) gas adsorption apparatus, the total specific pore volume is obtained by assuming that the condensed gas inside the pores has the molar volume and density of the bulk liquid at the same operational temperature.[20] According to our result, this traditional approach will lead to slight underestimation of total pore volume of porous materials. Even though our observation was made for the methane in MCM41 and SBA15, it is still a reasonable speculation that this finding may be generally true for liquid confined in small nanometer-sized pores. Hence, for the liquid phase hydrocarbons in shale rock, about 9% difference of liquid density could be possible. Future works need to be performed to experimentally verify this. In addition, our results seem to indicate that the liquid methane density is smaller in smaller pore as the density in CD_4/MCM-41 is smaller than that in CD_4/SBA-15. But as the

DOI: 10.1021/acs.langmuir.6b02291
Langmuir 2016, 32, 8849−8857

pore size is so small, it is likely that the surface structure may also play a role here. The detailed reasons still need some future studies.

Figure 3c indicates that in both CD_4/MCM-41 and CD_4/SBA-15 cases, the density of confined methane increases with the decreasing temperature when $T < T_c$. We notice that the trend of the density change with temperature is different in these two cases. For CD_4/SBA-15, the density has a sharp transition at $T \approx 65$ K, below which the density maintains roughly as a constant. A methane liquid−solid transition may take place at this temperature. In contrast, for CD_4/MCM-41, the methane density increases continuously with decreasing temperature and eventually reaches a plateau at $T < 30$ K. The mechanism behind these different trends is not clear yet even though it may be related to the pore size effect. Future simulations or theoretical works may help to clarify this phenomenon. Also, we need to be careful to generalize the density difference observed in MCM-41 and SBA-15 to the pure pore size effect. The solid density of methane in small pores depends on many factors, such as the pore size and the surface structure. Especially, due to the finite size, the nucleation growth of solid methane is restricted. Even the diffusion of the methane in pores may play a role as well. Unlike the liquid methane, the diffusion of the solid methane may be very slow. This may make it very slow for a system to reach the equilibrium. A future study is needed to understand the factors affecting the solid methane formation in small pores.

For $T > T_c$, our previous work[34] showed that the vapor core radius R_v (and therefore the thickness of adsorbed layer) and the density of adsorbed CD_4 before the gas−liquid condensation are sometimes coupled together and their absolute values depend on the density profile of solid matrix being used. Therefore, a more reliable parameter is excess adsorption rather than R_v and adsorbed gas density. The specific absolute adsorption M_{ads}, i.e. the absolute adsorption per volume of a single pore, is calculated by $M_{ads} = \int_0^\infty \rho_{CD_4,mass}\varphi_{GA}(r)2\pi r dr/CS$, where $\varphi_{GA}(r)$ is the gas accessible volume fraction and $CS = \int_0^\infty \varphi_{GA}(r)2\pi r dr$ is the cross section of a mesopore. M_{ads} versus temperature is plotted in Figure 3d. This adsorption is an indication of the statistically averaged adsorption behavior of all mesopores. Since adsorption is an exothermic reaction, decreasing temperature should increase the amount of gas adsorption as shown in Figure 3d. Interestingly, at $T > T_c$, M_{ads} is larger for SBA-15 than MCM-41. The larger adsorption amount in the larger pore (SBA-15) found here is different from that predicted from previous grand canonical Monte Carlo (GCMC) simulation[27] and molecular dynamics (MD) simulation.[26] Mosher et al.[27] carried out GCMC simulation on isotherms of methane adsorption in noninterconnected, graphitic slit pores with pore size ranging from 4 to 90 Å and found that the smaller pore adsorbs more methane at 298 K and at pressure smaller than 18 000 kPa. Similarly, Zhu and Zhao[26] did MD simulation on methane isotherm adsorption in carbon nanotubes (CNTs) with diameter from 9 to 32 Å and found that when CNT has diameter larger than 20 Å, smaller CNT has higher methane adsorption below 30 000 kPa. It should be noticed that Figure 3d plots the specific absolute adsorption M_{ads} of CD_4 within "a single mesopore". At $T > T_c$, M_{ads} is governed by the surface roughness of the pore wall and the interaction between the solid matrix and the gas molecules. Since both MCM-41 and SBA-15 are mesoporous silicas, the interaction of solid matrix and CD_4 is similar for both cases[47] despite some subtle difference in the surface structures due to different synthesis methods.[48] As a result, M_{ads} in CD_4/SBA-15 is much higher than M_{ads} in CD_4/MCM-41 due to large surface roughness of SBA-15 (see σ/R_m in Table 2). This is consistent with the large volume fraction of micropores on the pore wall of SBA-15 matrix found previously.[35,45] Therefore, the surface roughness, rather than the pore size, is the dominant parameter to determine the surface adsorption amount for the pores before the gas−liquid condensation temperature in the cases studied here. The important role of surface roughness on the states of adsorbed fluids such as krypton[18] and *n*-pentane and perfluoropentane[49] in SBA-15 had also been discussed in previous studies using different matrix density profiles. It will be interesting to compare the adsorption behavior of different gas molecules in the future work.

We notice that even though the gas−liquid condensation has a very sharp transition as seen by the dramatic intensity decrease close to the condensation temperature, the intensity change still spans a narrow temperature range. This may be due to the slight difference of the surface roughness of different pores and some polydispersity of the pore size. We thus further define $T_{c,L}$ and $T_{c,H}$ as the lowest and the highest temperatures for this condensation temperature range, i.e., the temperature range for first-order peak intensity shown in Figure 3a drops abruptly (117 K $\leq T \leq$ 132 K for MCM-41 and 112 K $\leq T \leq$ 119 K for SBA-15). $T_{c,L}$ and $T_{c,H}$ thus are useful parameters to understand the mechanisms of the gas−liquid condensation in the pores. When the temperature reaches $T_{c,L}$, liquid CD_4 just fills the entire pores. $M_{ads}(T = T_{c,H})/M_{ads}(T = T_{c,L})$ is 0.368 and 0.584 for CD_4/MCM-41 and CD_4/SBA-15, respectively. The large value for both cases indicates that the rough surface can adsorb lots of gas prior to capillary condensation. Hence, the surface roughness plays an important role in determining the gas adsorption properties. The real shale rock may have even more surface roughness than the model silica mesoporous materials being studied here. After the gas−liquid condensation takes place, M_{ads} equals the mass density of CD_4 confined in the mesopores and becomes similar for both CD_4/MCM-41 and CD_4/SBA-15 (see Figure 3c).

CONCLUSIONS

Temperature-dependent methane gas adsorption in mesoporous silica materials with different pore sizes is studied by small-angle neutron scattering technique. As far as we know, this is the first neutron scattering study of the pore size influence on the temperature-dependent gas adsorption process (close to isobar condition with the methane pressure ≈100 kPa). Despite the large pore size difference between MCM-41 (nominal pore radius R_m of 16.5 Å) and SBA-15 (R_m of 34.1 Å), the average adsorption layer thickness at the temperature above the gas−liquid condensation temperature ($T > T_c$) is found to be similar in both samples. The adsorbed layer thickness in the materials is governed mainly by the surface roughness of the pore wall determined by many factors such as the surface defects and surface undulation. The existence of the surface roughness region also indicates that we have to be cautious when understanding the volumetric or gravimetric gas isotherm adsorption curves using the models based on smooth pore surfaces. Not surprisingly, the gas−liquid condensation takes place at a higher temperature for MCM-41 with smaller pores

DOI: 10.1021/acs.langmuir.6b02291
Langmuir 2016, 32, 8849−8857

than for SBA-15 as the smaller pores tend to condense gas molecules at higher temperatures.

The mass density of methane confined in both MCM-41 and SBA-15 for $T < Tc$ is determined in a wide range of temperatures. The density in confined space is found to be appreciably smaller than the corresponding bulk methane density at similar conditions. With decreasing temperature, the density increases and there is a sharp increase of the methane density in SBA-15 at $T \approx 65$ K, which is likely due to the liquid−solid transition. The methane density becomes almost constant after the temperature is below 65 K. However, this sharp transition of the methane density is not observed in MCM-41 which has a much smaller pore size. Instead, we see almost a continuous density increase when the temperature decreases. Only when the temperature is below 30 K does the methane density in MCM-41 become almost a constant value. The difference in liquid density behavior in MCM-41 and SBA-15 is very likely induced by the different pore sizes. The exact mechanisms need to be further investigated in the future.

In most of the porosity measurements using the popular Sieverts method, one of the fundamental assumptions is that when the gas−liquid condensation happens, the liquid density confined in porous materials is the same as the bulk liquid density. However, our experimental results indicate that in nanometer-sized pores, the confined density can be different from the bulk density by an appreciable amount. Therefore, the traditional method may slightly underestimate the available pore volume in a porous material even though the difference is not too big based on our results.

The total adsorption within a single mesopore is determined as a function of temperature. It confirms our previous work that surface roughness plays an important role in the amount of surface adsorption prior to the capillary condensation. Therefore, the surface properties of the pores such as surface roughness and the surface chemistry, rather than the pore size, should be the most essential parameters to determine the total adsorption within the pores in materials with large surface roughness.

■ ASSOCIATED CONTENT

Supporting Information

The Supporting Information is available free of charge on the ACS Publications website at DOI: 10.1021/acs.langmuir.6b02291.

Scattering length density of empty matrices, temperature stability of empty matrices, CD_4 pressure versus temperature, N_2 adsorption isotherm, and sensitivity check of methane mass density (PDF)

■ AUTHOR INFORMATION

Corresponding Authors

*E-mail: jinhong.chen@aramcoservices.com. Tel.: (+1)713-432-4999.

*E-mail: yunliu@nist.gov. Tel.: (+1)301-975-6235. Fax: (+1) 301-921-9847.

Notes

The authors declare no competing financial interest.

■ ACKNOWLEDGMENTS

The authors thank Ronald Jones, Kathleen Weigandt, Tanya Dax, Alan Ye, and Juscelino Leao for the *n*Soft beamline support. We also thank Dr. Dan Georgi for his support of the project. Furthermore, Dr. Jorge Tovar is acknowledged for help with sorption isotherm experiments. Y.L. acknowledges the partial support of cooperative agreements 70NANB12H239 and 70NANB10H256 from NIST, U.S. Department of Commerce. This work was funded in part by Aramco Services Company and utilized facilities supported in part by the National Science Foundation under Agreement No. DMR-0944772. E.F. and P.B. kindly acknowledge CSGI for partial financial support.

■ REFERENCES

(1) Mastalerz, M.; He, L.; Melnichenko, Y. B.; Rupp, J. A. Porosity of Coal and Shale: Insights from Gas Adsorption and SANS/USANS Techniques. *Energy Fuels* **2012**, *26*, 5109−5120.

(2) Clarkson, C. R.; Solano, N.; Bustin, R. M.; Bustin, A. M. M.; Chalmers, G. R. L.; He, L.; Melnichenko, Y. B.; Radliński, A. P.; Blach, T. P. Pore Structure Characterization of North American Shale Gas Reservoirs Using USANS/SANS, Gas Adsorption, and Mercury Intrusion. *Fuel* **2013**, *103*, 606−616.

(3) Ruppert, L. F.; Sakurovs, R.; Blach, T. P.; He, L.; Melnichenko, Y. B.; Mildner, D. F. R.; Alcantar-Lopez, L. A USANS/SANS Study of the Accessibility of Pores in the Barnett Shale to Methane and Water. *Energy Fuels* **2013**, *27*, 772−779.

(4) U.S. energy-shale gas production 2015; Statistic http://www.statista.com/statistics/183740/shale-gas-production-in-the-united-states-since-1999/ (accessed May 20, 2016).

(5) Shale gas provides largest share of U.S. natural gas production in 2013. Today in Energy—U.S. Energy Information Administration (EIA) http://www.eia.gov/todayinenergy/detail.cfm?id=18951 (accessed May 20, 2016).

(6) Ambrose, R. J.; Hartman, R. C.; Diaz Campos, M.; Akkutlu, I. Y.; Sondergeld, C. *New Pore-Scale Considerations for Shale Gas in Place Calculations*. In *SPE Unconventional Gas Conference*; Society of Petroleum Engineers, 2013.

(7) Loucks, R. G.; Reed, R. M.; Ruppel, S. C.; Jarvie, D. M. Morphology, Genesis, and Distribution of Nanometer-Scale Pores in Siliceous Mudstones of the Mississippian Barnett Shale. *J. Sediment. Res.* **2009**, *79*, 848−861.

(8) Corma, A. From Microporous to Mesoporous Molecular Sieve Materials and Their Use in Catalysis. *Chem. Rev.* **1997**, *97*, 2373−2420.

(9) Chang, F.; Zhou, J.; Chen, P.; Chen, Y.; Jia, H.; Saad, S. M. I.; Gao, Y.; Cao, X.; Zheng, T. Microporous and Mesoporous Materials for Gas Storage and Separation: A Review. *Asia-Pac. J. Chem. Eng.* **2013**, *8*, 618−626.

(10) Vartuli, J. C.; Schmitt, K. D.; Kresge, C. T.; Roth, W. J.; Leonowicz, M. E.; McCullen, S. B.; Hellring, S. D.; Beck, J. S.; Schlenker, J. L. Effect of Surfactant/Silica Molar Ratios on the Formation of Mesoporous Molecular Sieves: Inorganic Mimicry of Surfactant Liquid-Crystal Phases and Mechanistic Implications. *Chem. Mater.* **1994**, *6*, 2317−2326.

(11) Beck, J. S.; Vartuli, J. C.; Roth, W. J.; Leonowicz, M. E.; Kresge, C. T.; Schmitt, K. D.; Chu, C. T. W.; Olson, D. H.; Sheppard, E. W.; McCullen, S. B.; Higgins, J. B.; Schlenker, J. L. A New Family of Mesoporous Molecular Sieves Prepared with Liquid Crystal Templates. *J. Am. Chem. Soc.* **1992**, *114*, 10834−10843.

(12) Kresge, C. T.; Leonowicz, M. E.; Roth, W. J.; Vartuli, J. C.; Beck, J. S. Ordered Mesoporous Molecular Sieves Synthesized by a Liquid-Crystal Template Mechanism. *Nature* **1992**, *359*, 710−712.

(13) Sayari, A.; Yang, Y.; Kruk, M.; Jaroniec, M. Expanding the Pore Size of MCM-41 Silicas: Use of Amines as Expanders in Direct Synthesis and Postsynthesis Procedures. *J. Phys. Chem. B* **1999**, *103*, 3651−3658.

(14) Neimark, A.; Ravikovitch, P.; Grün, M.; Schüth, F.; Unger, K. Pore Size Analysis of MCM-41 Type Adsorbents by Means of Nitrogen and Argon Adsorption. *J. Colloid Interface Sci.* **1998**, *207*, 159−169.

DOI: 10.1021/acs.langmuir.6b02291
Langmuir 2016, 32, 8849−8857

(15) Ravikovitch, P. I.; Neimark, A. V. Characterization of Nanoporous Materials from Adsorption and Desorption Isotherms. *Colloids Surf., A* **2001**, *187−188*, 11−21.
(16) Muroyama, N.; Yoshimura, A.; Kubota, Y.; Miyasaka, K.; Ohsuna, T.; Ryoo, R.; Ravikovitch, P. I.; Neimark, A. V.; Takata, M.; Terasaki, O. Argon Adsorption on MCM-41 Mesoporous Crystal Studied by In Situ Synchrotron Powder X-ray Diffraction. *J. Phys. Chem. C* **2008**, *112*, 10803−10813.
(17) Miyasaka, K.; Neimark, A. V.; Terasaki, O. Density Functional Theory of in Situ Synchrotron Powder X-ray Diffraction on Mesoporous Crystals: Argon Adsorption on MCM-41. *J. Phys. Chem. C* **2009**, *113*, 791−794.
(18) Hofmann, T.; Wallacher, D.; Huber, P.; Birringer, R.; Knorr, K.; Schreiber, A.; Findenegg, G. Small-Angle X-ray Diffraction of Kr in Mesoporous Silica: Effects of Microporosity and Surface Roughness. *Phys. Rev. B: Condens. Matter Mater. Phys.* **2005**, *72*, 064122.
(19) Zickler, G.; Jähnert, S.; Wagermaier, W.; Funari, S.; Findenegg, G.; Paris, O. Physisorbed Films in Periodic Mesoporous Silica Studied by in Situ Synchrotron Small-Angle Diffraction. *Phys. Rev. B: Condens. Matter Mater. Phys.* **2006**, *73*, 184109.
(20) Rouquerol, J.; Rouquerol, F.; Llewellyn, P.; Maurin, G.; Sing, K. S. W. *Adsorption by Powders and Porous Solids: Principles, Methodology and Applications*; Academic Press: New York, 2013.
(21) Gregg, S. J.; Sing, K. S. W. *Adsorption, Surface Area, and Porosity*; Academic Press: New York, 1991.
(22) Gor, G. Y.; Siderius, D. W.; Rasmussen, C. J.; Krekelberg, W. P.; Shen, V. K.; Bernstein, N. Relation between Pore Size and the Compressibility of a Confined Fluid. *J. Chem. Phys.* **2015**, *143*, 194506.
(23) Jiang, J.; Sandler, S. I.; Smit, B. Capillary Phase Transitions of N-Alkanes in a Carbon Nanotube. *Nano Lett.* **2004**, *4*, 241−244.
(24) Tan, S. P.; Piri, M. Equation-of-State Modeling of Confined-Fluid Phase Equilibria in Nanopores. *Fluid Phase Equilib.* **2015**, *393*, 48−63.
(25) Islam, A. W.; Patzek, T. W.; Sun, A. Y. Thermodynamics Phase Changes of Nanopore Fluids. *J. Nat. Gas Sci. Eng.* **2015**, *25*, 134−139.
(26) Zhu, X.; Zhao, Y.-P. Atomic Mechanisms and Equation of State of Methane Adsorption in Carbon Nanopores. *J. Phys. Chem. C* **2014**, *118*, 17737−17744.
(27) Mosher, K.; He, J.; Liu, Y.; Rupp, E.; Wilcox, J. Molecular Simulation of Methane Adsorption in Micro- and Mesoporous Carbons with Applications to Coal and Gas Shale Systems. *Int. J. Coal Geol.* **2013**, *109−110*, 36−44.
(28) Dong, X.; Liu, H.; Hou, J.; Wu, K.; Chen, Z. Phase Equilibria of Confined Fluids in Nanopores of Tight and Shale Rocks Considering the Effect of Capillary Pressure and Adsorption Film. *Ind. Eng. Chem. Res.* **2016**, *55*, 798−811.
(29) Qiao, S. Z.; Bhatia, S. K.; Zhao, X. S. Prediction of Multilayer Adsorption and Capillary Condensation Phenomena in Cylindrical Mesopores. *Microporous Mesoporous Mater.* **2003**, *65*, 287−298.
(30) Kruk, M.; Jaroniec, M. Determination of Mesopore Size Distributions from Argon Adsorption Data at 77 K. *J. Phys. Chem. B* **2002**, *106*, 4732−4739.
(31) Zhu, H. Y.; Ni, L. A.; Lu, G. Q. A Pore-Size-Dependent Equation of State for Multilayer Adsorption in Cylindrical Mesopores. *Langmuir* **1999**, *15*, 3632−3641.
(32) Qiao, S. Z.; Bhatia, S. K.; Nicholson, D. Study of Hexane Adsorption in Nanoporous MCM-41 Silica. *Langmuir* **2004**, *20*, 389−395.
(33) Morishige, K.; Nakamura, Y. Nature of Adsorption and Desorption Branches in Cylindrical Pores. *Langmuir* **2004**, *20*, 4503−4506.
(34) Chiang, W.-S.; Fratini, E.; Baglioni, P.; Georgi, D.; Chen, J.; Liu, Y. Methane Adsorption in Model Mesoporous Material, SBA-15, Studied by Small-Angle Neutron Scattering. *J. Phys. Chem. C* **2016**, *120*, 4354−4363.
(35) Impéror-Clerc, M.; Davidson, P.; Davidson, A. Existence of a Microporous Corona around the Mesopores of Silica-Based SBA-15 Materials Templated by Triblock Copolymers. *J. Am. Chem. Soc.* **2000**, *122*, 11925−11933.
(36) Tanaka, H.; Hiratsuka, T.; Nishiyama, N.; Mori, K.; Miyahara, M. T. Capillary Condensation in Mesoporous Silica with Surface Roughness. *Adsorption* **2013**, *19*, 631−641.
(37) Beachell, H. C.; Veloric, H. S. Adsorption Isotherms, Isobars, and Isosteres of Diborane on Boron Nitride and Palladium on Charcoal. *J. Phys. Chem.* **1956**, *60*, 102−103.
(38) Kuhn, W. K.; Szanyi, J.; Goodman, D. W. Adsorption Isobars for CO on Pd/Ta(110) at Elevated Pressures and Temperatures Using Infrared Reflection-Absorption Spectroscopy. *Surf. Sci.* **1994**, *303*, 377−385.
(39) Rey, L.; Gambaro, L. A.; Thomas, H. J. Oxygen Chemisorption on V_2O_5: Isotherms and Isobars of Adsorption. *J. Catal.* **1984**, *87*, 520−523.
(40) Ritter, H.; Nieminen, M.; Karppinen, M.; Brühwiler, D. A Comparative Study of the Functionalization of Mesoporous Silica MCM-41 by Deposition of 3-Aminopropyltrimethoxysilane from Toluene and from the Vapor Phase. *Microporous Mesoporous Mater.* **2009**, *121*, 79−83.
(41) Identification of a commercial product does not imply recommendation or endorsement by the national institute of standards and technology, nor does it imply that the product is necessarily the best for the stated purpose.
(42) Zhao, D.; Feng, J.; Huo, Q.; Melosh, N.; Fredrickson, G. H.; Chmelka, B. F.; Stucky, G. D. Triblock Copolymer Syntheses of Mesoporous Silica with Periodic 50 to 300 Angstrom Pores. *Science (Washington, DC, U. S.)* **1998**, *279*, 548−552.
(43) Lowell, S.; Shields, J. E.; Thomas, M. A.; Thommes, M. *Mesopore Analysis*; Springer: Dordrecht, Netherlands, 2004; pp 101−128.
(44) Kline, S. R. Reduction and Analysis of SANS and USANS Data Using IGOR Pro. *J. Appl. Crystallogr.* **2006**, *39*, 895−900.
(45) Galarneau, A.; Cambon, H.; Di Renzo, F.; Ryoo, R.; Choi, M.; Fajula, F. Microporosity and Connections between Pores in SBA-15 Mesostructured Silicas as a Function of the Temperature of Synthesis. *New J. Chem.* **2003**, *27*, 73−79.
(46) Setzmann, U.; Wagner, W. A New Equation of State and Tables of Thermodynamic Properties for Methane Covering the Range from the Melting Line to 625 K at Pressures up to 100 MPa. *J. Phys. Chem. Ref. Data* **1991**, *20*, 1061.
(47) Makowski, W.; Mańko, M.; Dudek, A.; Mlekodaj, K. Application of Quasi-Equilibrated Thermodesorption of Hexane and Cyclohexane for Characterization of Porosity of Zeolites and Ordered Mesoporous Silicas. *Adsorption* **2013**, *19*, 537−544.
(48) Ide, M.; El-Roz, M.; De Canck, E.; Vicente, A.; Planckaert, T.; Bogaerts, T.; Van Driessche, I.; Lynen, F.; Van Speybroeck, V.; Thybault-Starzyk, F.; et al. Quantification of Silanol Sites for the Most Common Mesoporous Ordered Silicas and Organosilicas: Total versus Accessible Silanols. *Phys. Chem. Chem. Phys.* **2013**, *15*, 642−650.
(49) Findenegg, G. H.; Jähnert, S.; Müter, D.; Prass, J.; Paris, O.; Acatrinei, A. I.; Hartl, M. A.; Eckert, J.; Falcao, E. H. L.; Chertkov, G.; et al. Fluid Adsorption in Ordered Mesoporous Solids Determined by in Situ Small-Angle X-Ray Scattering. *Phys. Chem. Chem. Phys.* **2010**, *12*, 7211.

DOI: 10.1021/acs.langmuir.6b02291
Langmuir 2016, 32, 8849−8857